Impact of Axial Load on the Seismic Response of Rectangular Walls

Alex V. Shegay, S.M.ASCE[1]; Christopher J. Motter, Ph.D., P.E.[2]; Kenneth J. Elwood, Ph.D., P.E.[3]; Richard S. Henry, Ph.D.[4]; Dawn E. Lehman, Ph.D., A.M.ASCE[5]; and Laura N. Lowes, Ph.D., A.M.ASCE[6]

Abstract: Experimental testing was conducted on four large-scale, flexure-yielding walls with rectangular cross sections to investigate the impact of imposed axial load ratio (10, 14, and 20% of axial compression capacity) and transverse reinforcement detailing on the seismic performance, including damage and deformability. Variations in detailing included the inclusion or exclusion of crossties on web longitudinal reinforcement, the confined length of the boundary element, and the effectiveness of using full hoops versus 180–180° crossties in boundary elements. Failure was characterized by simultaneous crushing of the boundary element core concrete and buckling of the longitudinal reinforcement, except for one wall that failed by out-of-plane instability of the wall boundary element. The plastic rotations at lateral strength loss of 20% were on average 3.3, 2.7, and 2.1% for walls with axial load ratios of 0.1, 0.14, and 0.2, respectively. These rotations exceeded the codified limits used for assessment of structures in the United States but were below the codified limits used for design in New Zealand for axial load ratios exceeding 10%. A model for determining the plastic rotation capacity of rectangular walls as a function of the axial load is proposed. **DOI: [10.1061/(ASCE)ST.1943-541X.0002122](#).** © *2018 American Society of Civil Engineers.*

Introduction

Reinforced concrete (RC) walls are commonly used as the lateral force resisting system in low- to high-rise buildings to meet the required strength and stiffness. Following the 2010/2011 Canterbury earthquakes in New Zealand and the 2010 Maule earthquake in Chile, significant compressive damage was observed in RC walls. This included crushing of concrete [Fig. 1(a)] and local buckling of longitudinal reinforcement in the boundary elements (i.e., wall end region) and in the wall web (i.e., wall interior region) as shown in Fig. 1(b). In some cases, the damaged wall moved out-of-plane, as shown in Fig. 1(c). To better understand these observations, a study was undertaken to analyze prior research and test walls that investigated high axial demands and detailing to delay compressive damage in walls. The findings from this work were used to evaluate approaches used in concrete design codes to address compression demands and mitigate earthquake damage.

In New Zealand, wall damage after the 2010/2011 Canterbury earthquakes was used to identify potential shortcomings of the New Zealand Concrete Structures Standard (Amendment 2) NZS 3101:2006-A2 (NZS 2012). These findings were reported by the Canterbury Earthquakes Royal Commission (CERC 2012) and the Structural Engineering Society New Zealand (SESOC 2013), and led to implement new provisions in NZS 3101:2006-A3. Specific attention was given to the impact on wall performance of the confined length of the boundary element, longitudinal bar restraint in the plastic region of the wall, type of confinement (e.g., hoop versus crosstie), and axial load ratio ($P/A_g f'_c$, where P is the axial load, A_g is the gross cross-sectional area of the wall, and f'_c is the specified concrete strength). Prior research into the impact of these parameters and the identified research gaps are described subsequently.

The impact of boundary element detailing on compressive strain capacity has been investigated previously. To simplify the experimental program, researchers have used rectangular prism studies to simulate the boundary element of the wall (Arteta 2015; Hilson 2014; Mander et al. 1988; Welt et al. 2017). Following the Maule earthquake in Chile, Welt et al. (2017) demonstrated improved restraint provided by hoops versus crossties with 90 and 135° hooks. In New Zealand, 180° hooks are commonly used; however, no known wall studies and only one prism study (Mander et al. 1988) have investigated the effectiveness of 180–180° crossties compared to hoops. Welt et al. (2017) also demonstrated the importance of providing buckling restraint by corners of hoops or crossties to all boundary element longitudinal reinforcement.

Increasing the length of the confined region has been found previously to increase deformation capacity of walls in analytical (Whitman 2015) and experimental (Deng et al. 2008) studies. Deformation capacity has also been found to improve by providing restraint against buckling for web longitudinal reinforcement; buckling of web longitudinal reinforcement was observed in Christchurch (CERC 2012) and in tests (e.g., Huq et al. 2017; Lowes et al. 2012). All of these studies have investigated walls with high shear stress demands ($V_u/A_g > 0.4\sqrt{f'_{c,test}}$ MPa, where V_u is the maximum measured lateral force and $f'_{c,test}$ is the tested concrete compressive stress). Further research is required to quantify the impact of confinement length and longitudinal web reinforcement restraint on walls with low shear strength demands.

[1]Ph.D. Student, Dept. of Civil and Environmental Engineering, Univ. of Auckland, Auckland 1023, New Zealand (corresponding author). Email: alex.shegay@auckland.ac.nz

[2]Assistant Professor, Dept. of Civil and Environmental Engineering, Washington State Univ., Pullman, WA 99164.
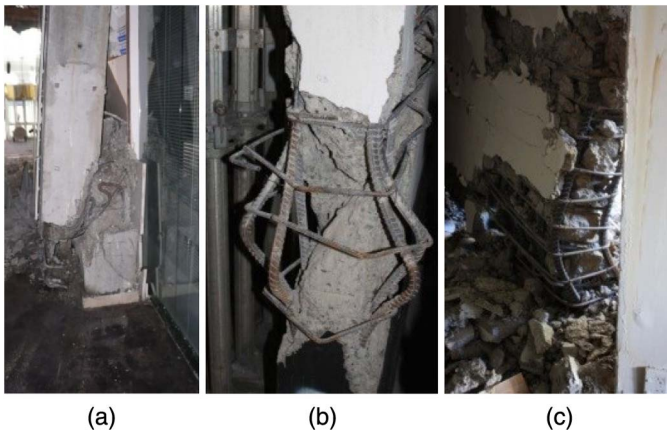
[3]Professor, Dept. of Civil and Environmental Engineering, Univ. of Auckland, Auckland 1023, New Zealand.

[4]Senior Lecturer, Dept. of Civil and Environmental Engineering, Univ. of Auckland, Auckland 1023, New Zealand.

[5]Professor, Dept. of Civil and Environmental Engineering, Univ. of Washington, Seattle, WA 98195-2700.

[6]Professor, Dept. of Civil and Environmental Engineering, Univ. of Washington, Seattle, WA 98195-2700.

Fig. 1. (a) Axial crushing (reprinted from Dunning Thornton Consultants Ltd. 2011); (b) boundary element crushing and reinforcement buckling (reprinted from NIST 2014); and (c) global out-of-plane instability.

seismicity in the United States and New Zealand, there is a need to quantify the impact of low-to-moderate axial load ratios (0.1–0.3) on wall deformation capacity.

While there was no axial load limit for ductile walls in NZS 3101:2006-A2, a limit of 0.3 has been recently adopted in the third amendment (A3) of NZS 3101:2006 (NZS 2017). Comparatively, a limit of 0.35 exists in the Canadian concrete structures design standard (CSA 2004) and DS 60 MINVU (Chilean Structural Standard 2010). Walls subjected to an axial load ratio above 0.35 are not considered effective in resisting seismic forces in ASCE 41-13 (ASCE 2014) seismic evaluations. A limit on the axial load ratio does not exist in ACI 318-14 (ACI 2014), although ASCE 7-10 defines a wall with an axial load as a bearing wall, resulting in a lower force reduction factor on the unreduced base shear demands. Although these examples suggest that the axial load ratio significantly impacts the seismic response of walls, few studies have focused solely on the variation of axial load ratios less than 0.3 within a testing program.

This paper presents the results of an experimental study on four walls with different axial load ratios and confinement characteristics. The paper concludes with a study on plastic hinge rotation capacity using the test data of this study combined with selected prior test data that focused on axial load ratio and confinement detailing, as presented in Table 1.

Experimental Program

Overview

The test program consisted of four walls designed to study the impact of boundary element and web confinement detailing and low-to-moderate axial load ratio on the seismic performance of well-detailed, flexure-controlled planar walls. The one-half-scale, rectangular walls were constructed and tested at the University of Auckland Structural Testing Laboratory. Table 2 summarizes the design variables for the four walls. Test wall IDs indicate the confinement detailing characteristics (either Conventional detailing based on NZS 3101:2006-A2 or Augmented detailing with a longer confinement zone and crossties in the web region, based on NZS 3101:2006-A3) and the applied axial load ratio (e.g., C10 was designed with Conventional detailing according to NZS 3101:2006-A2 and subjected to an axial load ratio of 0.10, calculated using $f'_{c,test}$, the measured concrete compressive strength).

Large databases of planar wall tests (Lowes et al. 2012; Shegay et al. 2015) indicate that the vast majority of the tests have been subjected to axial load ratios less than 0.1. The few studies that have focused on the impact of axial load ratio on the drift capacity (Alarcon et al. 2014; Su and Wong 2007; Zhang and Wang 2000) have tested walls that do not fully meet ACI 318-14 special boundary element (SBE) requirements or NZS 3101:2006 boundary element transverse reinforcement requirements for ductile class walls. Parameters of the tested walls are listed in Table 1, including geometric ratios, axial load ratios, normalized shear stress demand, normalized neutral axis length, and measured drift and plastic rotation at 20% loss of lateral-load-carrying capacity. The plastic-rotation capacity was calculated assuming all plastic deformation occurred at the base of the wall within a height of $0.5L_w$, where L_w is the horizontal length of the wall, ranging from 400 to 1,000 mm for the studies in Table 1. It is evident from the data in Table 1 that drift capacity decreases with increasing axial load ratio. Drift capacity varies between 1.2 and 2.7% with values less than 1.7% measured for walls with axial load ratios between 0.30 and 0.5. Axial load ratios above 0.35 are higher than what would typically be encountered in the United States or New Zealand construction. To understand the performance of walls in regions of high

Table 1. Summary of previous experimental tests on walls with varied axial load

Study	Wall	$\dfrac{P}{A_g f'_{c,test}}$	$\dfrac{V_u}{A_g\sqrt{f'_{c,test}}}$	$\dfrac{M}{VL_w}$[a]	L_w (mm)	$\dfrac{L_w}{t_w}$	$\dfrac{c}{L_w}$[b]	$\rho_{l,BE}$ (%)[c]	$\dfrac{s}{d_b}$[d]	Δ_u (%)[e]	θ_p (%)[f]
Alarcon et al. (2014)	W1	0.15	0.32	2.3	1,000	7	0.24	3.0	9	2.7	2.7
	W2	0.24	0.40	2.3	1,000	7	0.36	3.0	9	1.8	1.4
	W3	0.34	0.40	2.3	1,000	7	0.46	3.0	9	1.5	1.1
Su and Wong (2007)	W1	0.24	0.38	1.6	400	5	0.4	3.5	7.5	2.2	1.8
	W2	0.48	0.45	1.6	400	5	0.66	3.5	7.5	1.3	0.8
	W3	0.48	0.50	1.6	400	5	0.66	3.5	7.5	1.2	0.7
Zhang and Wang (2000)	SW7	0.24	0.52	2.1	1,000	7	0.33	6.2	3.6	2.1	2.0
	SW8	0.33	0.55	2.1	1,000	7	0.45	4.5	4.2	1.6	1.5
	SW9	0.23	0.72	2.1	1,000	7	0.33	13.0	3.8	2.1	2.1

[a]M/VL_w = shear span ratio of the wall.
[b]c = neutral axis depth calculated using measured material strength.
[c]$\rho_{l,BE}$ = longitudinal reinforcement ratio in the wall boundary element.
[d]s/d_b = vertical transverse reinforcement spacing to longitudinal bar diameter ratio.
[e]Δ_u = ultimate drift capacity determined as drift at 20% strength loss.
[f]θ_p = plastic rotation capacity corresponding to the ultimate drift.

© ASCE

J. Struct. Eng.

Table 2. Test variables investigated in this study

Wall	Axial load	Web ties	L_c/c[a] (%)
C10	$0.10A_g f'_{c,test}$[b]	No	75
A10	$0.10A_g f'_{c,test}$	Yes	100
A14	$0.14A_g f'_{c,test}$	Yes	108
A20	$0.20A_g f'_{c,test}$	Yes	110

[a]L_c/c = length of confined region/neutral axis depth.
[b]$f_{c,test}$ = tested concrete compressive strength.

Walls C10 and A10 were designed to investigate two key detailing changes (while keeping the axial load ratio constant at 0.1): (1) confinement of the full or partial neutral axis depth, c, and (2) restraint or lack of restraint for every web longitudinal reinforcing bar using 180–180° crossties. Walls A14 and A20, in combination with Wall A10, were designed to investigate the influence of increasing the axial load ratio from 0.1 to 0.14 and 0.2. The NZS 3101:2006-A3 limit of 0.3 on the axial load ratio was not achievable in the tests due to limitations of the actuator capacities and higher than anticipated concrete strengths on test days.

Test Wall Design

The geometry and design forces used to design the test walls were obtained from an analysis of an 8-story prototype building in Wellington, New Zealand, that used rectangular walls to resist lateral loading (New Zealand Concrete Society 1998). Design base moments and base shear forces were obtained from an equivalent lateral force (ELF) distribution over the height of the wall, as shown in Fig. 2. The shear strengths of the walls were capacity designed according to NZS 1170.5 (NZS 2004) to account for overstrength and dynamic-amplification effects. All of the walls had the same horizontal reinforcement based on the required shear strength of Wall A20. This approach resulted in shear stress demands (at nominal moment), $V_{@Mn}/A_g$, ranging from $0.16\sqrt{f'_c}$ to $0.21\sqrt{f'_c}$ MPa, as summarized in Table 3.

The test walls represented the lower two stories of the 8-story walls in the prototype building, constructed at one-half scale (Fig. 2). This resulted in walls that were 2,250 mm long (L_w), 200 mm thick (t_w), and 3,500 mm tall (h_w), with a top-to-base moment ratio (M_{top}/M_{base}) of 0.57 and an effective height-to-length ratio (H_{eff}/L_w) of 4.6. A foundation block cast at the base of
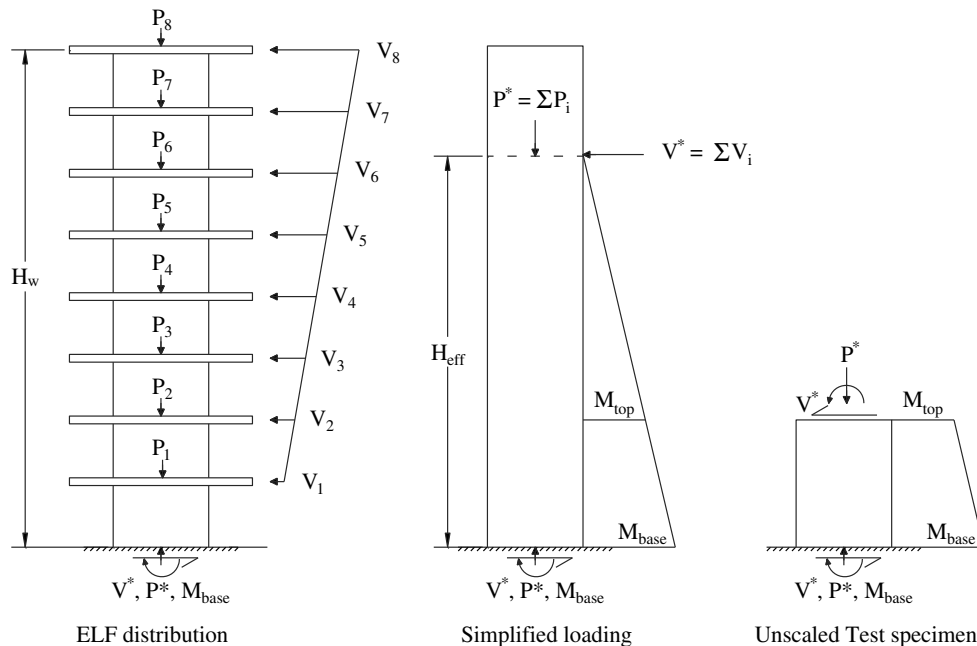
Fig. 2. Derivation of test wall loading.

Table 3. Wall strength and reinforcement properties

Wall	V_n (kN)[a]	M_n (kNm)[a]	M_{cr} (kNm)[b]	M_y (kNm)[c]	$\dfrac{V@M_n}{A_g\sqrt{f'_c}}$ (MPa)	$\rho_{l,e}$[d]	$\rho_{l,web}$[e]	c/L_w[f]	$A_{sh,provided}/A_{sh,required}$[g]
C10	1,384	3,962	1,074	3,472	0.16	0.027	0.0052	0.23	1.06
A10	1,390	3,962	1,097	3,472	0.16	0.022	0.0050	0.23	0.94
A14	1,474	5,025	1,673	4,380	0.20	0.016	0.0046	0.28	0.97
A20	1,544	5,285	2,188	5,176	0.21	0.013	—	0.34	0.95

[a]All nominal values have been calculated according to NZS 3101:2006-A3 and using measured material strengths.
[b]M_{cr} = theoretical moment at first cracking.
[c]M_y = theoretical moment at first yield of outermost longitudinal reinforcement.
[d]$\rho_{l,e}$ = longitudinal reinforcement ratio in the *confined* end region.
[e]$\rho_{l,web}$ = longitudinal reinforcement ratio in the web, between confined end regions.
[f]c = neutral axis depth calculated using measured material strengths.
[g]$A_{sh,provided}/A_{sh,required}$ = total area of transverse reinforcement provided normalized by the area of transverse reinforcement required according to NZS 3101:2006-A3.

© ASCE

04018124-3

J. Struct. Eng.
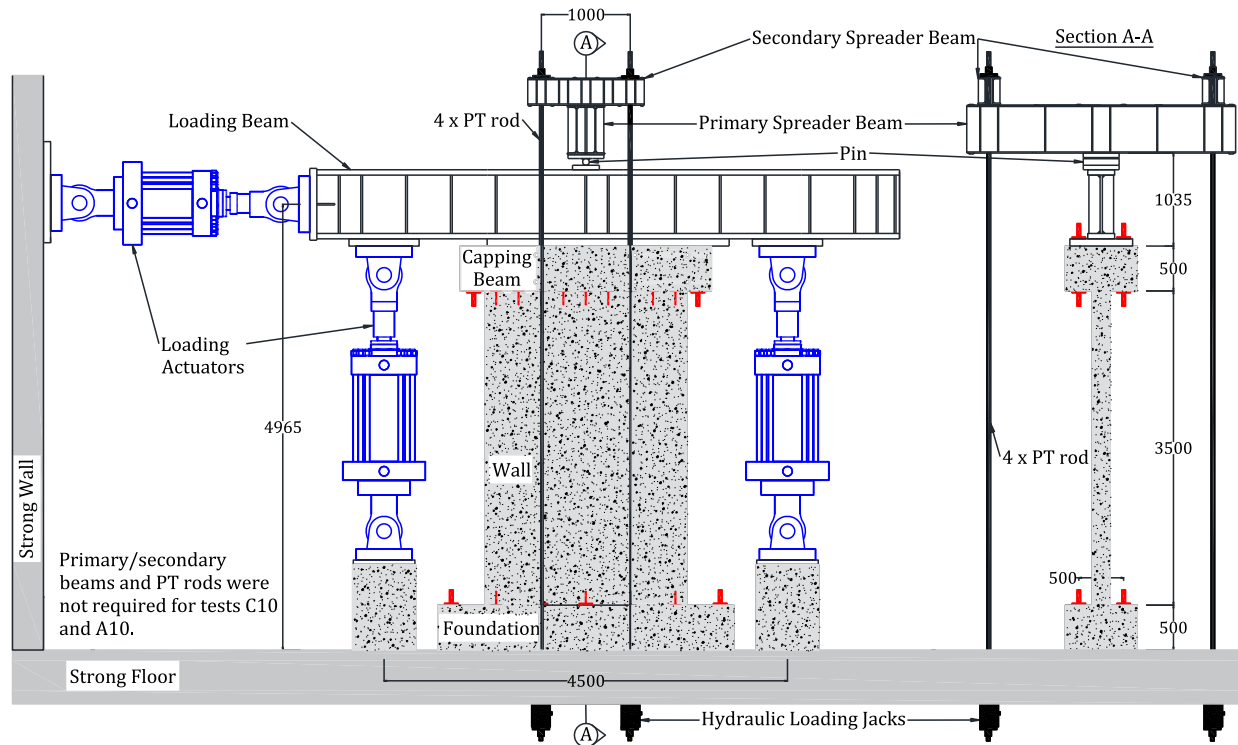
Fig. 3. Experimental test setup.

the wall and a capping beam cast at the top of the wall enabled fixity to the strong floor and the loading beam, respectively. The loading beam provided transfer of the applied axial load, moment, and shear forces to the wall, respectively (Fig. 3). Wall longitudinal reinforcement was anchored into the foundation and capping blocks using 90° hooks. The walls were cast in three concrete pours (foundation, wall panel, and capping block). The cold joint

interfaces between the three elements were roughened prior to subsequent pours.

The wall cross sections are presented in Fig. 4, and the reinforcement ratios and nominal strengths are summarized in Table 3. Longitudinal reinforcement and web horizontal reinforcement had surface deformations, while all transverse reinforcement was smooth (i.e., no surface deformations). In each wall, the boundary element

6/8/10/16 = Diameter in mm **H** = Grade 500E **D** = Deformed bar **R** = Round/Smooth bar
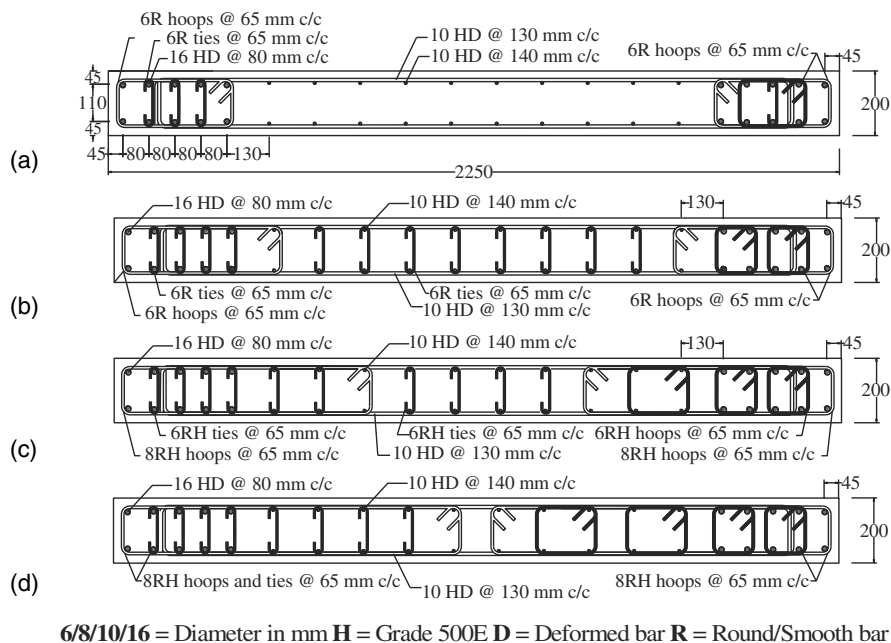
Fig. 4. Cross sections of test walls: (a) C10; (b) A10; (c) A14; and (d) A20. Locations of longitudinal reinforcement are the same for all walls.

Table 4. Comparison of test wall end region parameters to NZS 3101:2006-A2 and ACI 318-14 limits (accounting for scaling)

End region aspect	Provided in test walls	Percentage compliance NZS 3101:2006 (%)	Percentage compliance ACI 318-14 (%)
Section thickness	200 mm	97	91
Maximum spacing of unsupported longitudinal reinforcement	80 mm	125	167
Transverse reinforcement spacing to longitudinal bar diameter ratio	4.1	147	127
Transverse reinforcement ratio	0.005–0.007	94–110	50–130
Confined end region length	779–1,965 mm	99–110	130–140

Table 5. Mechanical properties of reinforcing steel and concrete

Bar diameter (mm)	Steel					Concrete		
	f_y (MPa)	ε_y	ε_{sh}[a]	f_u (MPa)[b]	ε_u[c]	Wall	$f'_{c,test}$ (MPa)	Strain at $f'_{c,test}$, e_0
6	393	0.0017	0.018	534	0.160	C10	32.7	−0.0026
8	519	0.0033	0.025	613	0.143	A10	32.7	−0.0026
10	507	0.005	0.012	653	0.123	A14	42.6	−0.0032
16	543	0.003	0.020	677	0.124	A20	43.7	−0.0032

[a]ε_{sh} = strain at which strain hardening begins.
[b]f_u = ultimate tensile strength, MPa.
[c]ε_u = strain at ultimate tensile strength.

detailing varied. One boundary element was confined using hoop reinforcement and the other boundary element was confined using a single hoop spanning the entire boundary element length with 180–180° crossties on every longitudinal bar, as is common in New Zealand practice. This permitted direct comparison of the two configurations of confinement reinforcement, both of which are compliant with NZS 3101:2006-A3 ductile plastic hinge region provisions and ACI 318-14 SBE provisions.

Table 4 further summarizes compliance of the boundary elements to NZS 3101:2006-A3 and ACI 318-14. A 65-mm vertical spacing of transverse reinforcement, s, was used for all four walls to meet requirements for the transverse reinforcement ratio. This led to s/d_b of 4.1, where d_b is the diameter of the longitudinal reinforcement. This s/d_b value is smaller than the NZS 3101:2006-A3 and ACI 318-14 requirements, as shown in Table 4.

Table 5 presents material properties determined from laboratory testing. The specified concrete compressive strength, f'_c, was 30 MPa. Deformed Grade 500E (New Zealand) steel was used for all longitudinal and web transverse reinforcement (average tested values of $f_y = 543$ MPa and $\varepsilon_u = 12\%$) and a combination of smooth Grades 500E and 300E (New Zealand) steel (average tested values of $f_y = 393$ MPa, $\varepsilon_u = 16\%$) was used for confinement reinforcement. Detailed material test data can be found in Shegay et al. (2018).

Test Set Up

Fig. 3 shows the test setup. Using high-strength threaded rods, the wall foundation block was post-tensioned to the laboratory strong floor and a structural steel loading beam was post-tensioned to the wall capping beam. Axial load and moment were applied through two vertical actuators on either side of the wall that were connected to the loading beam and the strong floor. Walls A14 and A20 were subjected to additional axial load that was applied using hydraulic jacks and post-tensioning rods. The servocontrolled actuators were programmed to autonomously adjust the axial load to compensate for any changes in the post-tensioning rod forces throughout the test. The post-tensioning rods were anchored to the strong floor and were connected at the top of the wall with a set of spreader beams. The spreader beams were

supported by a pin on top of the main loading beam that allowed free rotation of the spreader beams about the transverse axis of the wall.

Fig. 5 shows the external instrumentation layout for the test walls. As shown in Fig. 5, the walls were subdivided into three panel regions, each with a different instrumentation layout. Displacements were measured between indicated locations using displacement transducers called portal gauges (PGs). The PGs were installed vertically up the height of the walls and were anchored by inserts that were cast through the thickness of the wall during construction. The PG recordings were used to calculate the average curvature distribution up the height of the wall, which, in turn, was used to determine flexural deformation components. Diagonal PG measurements were used to determine shear deformations. Two additional PGs, one at each end of the wall, were installed to measure displacement between the foundation and a location 30–50 mm above the base of the wall (PGE and PGW in Fig. 5). The rotation derived from the difference into these displacements was assumed to be fully attributed to strain penetration of the longitudinal reinforcement into the wall and foundation. Additional information about external and internal instrumentation is provided in Shegay et al. (2018).

Unless otherwise stated, all reported drifts in this paper are the horizontal displacement measured at the top of the wall (which corresponds to the top of the 2nd story of the prototype building) divided by the height of the measuring instrument from the top of the foundation block. The loading protocol used in each test comprised two displacement-controlled cycles at a loading rate of 0.2 mm/s for peak drifts of 0.0625, 0.125, 0.25, 0.5, 0.75, 1.0, 1.5, 2.0, and 3.0%. Cyclic increments used beyond the 0.5% drift (corresponding to the first yield of longitudinal reinforcement, determined from plane-section fiber analysis) were consistent with criteria outlined in ACI ITG5.1-07 (ACI 2007). The walls sustained one or both of the following failure modes: *lateral-load failure*, which was defined as a 20% reduction of lateral-load-carrying capacity from maximum strength and/or *axial failure*, defined as the point at which the applied axial load could no longer be sustained. After lateral-load failure occurred, the walls were monotonically pushed to achieve one or both failure modes in the opposite direction.
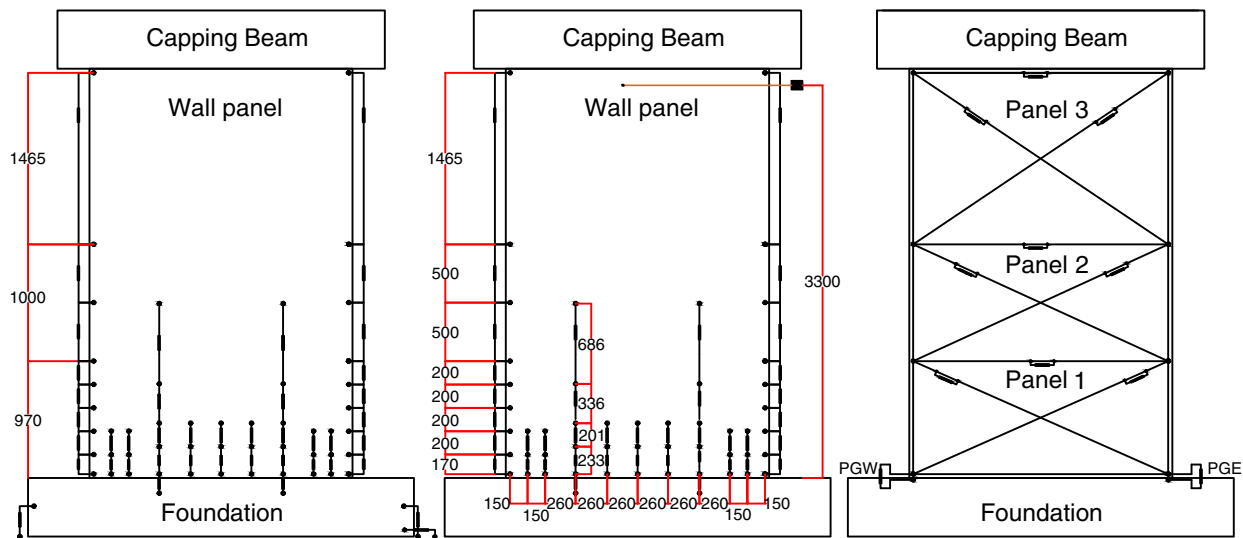
Fig. 5. External instrumentation layout for each wall.

Damage Progression

The damage progression for each wall is summarized in Table 6. Photos of the boundary-element damage states at measured drifts of 1.0, 1.5%, and at lateral-load failure, respectively, are shown in Figs. 6–8. The base moment-drift response for each wall, without inclusion of P-delta effects, is shown in Fig. 9. Maximum shear and moment sustained by each wall, as well as measured drift at the onset of cracking, first yield of longitudinal reinforcement, and lateral-load failure, is provided in Table 7. For comparison to results from other test programs, the drift at effective height (10.35 m above the wall base) is also provided in Table 7, in parentheses in Table 6, and along the top axis in Fig. 9. This drift was calculated using an effective stiffness of $0.35EI_g$ [ACI 318-14 (ACI 2014); NZS 3101:2006 (NZS 2017)] and assuming no additional plastic deformation above the test wall height.

For all walls, damage, as documented in Table 6, progressed as follows:

Cracking
Horizontal (i.e., flexural) cracking initiated at drifts between 0.125 and 0.25%; horizontal cracks were observed up the full height of the wall by 0.5% drift. Maximum residual crack widths (MRC) were less than 0.2 mm for cycles below 0.75% drift and increased to a maximum of 2.5 mm for Walls C10, A10, and A14 and 1.4 mm for A20 at 2.0% drift.

Spalling
Spalling initiated at 1.0% drift for Walls C10, A10, and A14 and at 0.75% drift for Wall A20 (Fig. 6). Prior to wall lateral-load failure (at 3.1% drift), the spalled region extended 1,000 mm up the height and 400 mm along the length of Walls C10 and A10. In Walls A14 and A20, the spalled region extended 1,300 mm up the height prior to failure (at 2.5 and 2.0% drift, respectively) and 500 and 700 mm along the length of the wall, respectively.

Bar Buckling
First observations of out-of-plane movement of longitudinal reinforcement were observed at the completion of 2.0% drift cycles for Walls C10 and A14, with significant buckling not occurring until lateral-load failure. In Wall A10, peripheral DH16 bars buckled at 600 mm above the base of the foundation at 3.0% drift and over a height of four transverse hoops; however, the wall did

not move out-of-plane or experience lateral-load failure at this drift level. Highly localized buckling of the corner bars was observed in Walls A14 and A20 during lateral-load failure. The buckling occurred over a single hoop spacing [Fig. 8(c)] at heights varying between 300 and 500 mm above the wall base.

Bar Fracture
Fracture of longitudinal reinforcement did not occur prior to lateral-load failure in any of the tested walls. Following lateral-load failure, previously buckled longitudinal reinforcement fractured in Walls C10, A10, and A14. For all walls, fracture of transverse reinforcement was observed at both ends of the wall after lateral-load failure, with fracture of more hoop legs than crosstie legs for a given wall. Axial failure occurred concurrently with additional fracture of transverse reinforcement.

Failure

For all walls, loss of lateral-load-carrying capacity occurred prior to loss of axial capacity. For three of four walls (C10, A14, and A20), lateral-strength loss at lateral-load failure was immediate because of a compression failure characterized by simultaneous crushing of confined concrete and buckling of longitudinal reinforcement. For Wall A10, lateral-load failure was more gradual with increasing drift demand as a result of large out-of-plane movement of the compression region of the wall; failure is classified as an out-of-plane instability failure. For all walls, axial-load-carrying capacity was maintained after lateral-load failure, with axial failure occurring only after load reversal from the point of lateral-load failure. Summary of lateral and axial failure for each wall are presented subsequently.

Lateral-Load Failure
Wall C10 experienced a lateral-load failure at −3.1% drift due to crushing of the confined end region core concrete and simultaneous buckling of the outermost compression longitudinal reinforcement [Fig. 8(a)]. Wall A10 sustained lateral-load-carrying capacity when loaded to −3.1% drift despite exhibiting significant buckling of the outer DH16 reinforcement bars; lateral-load failure occurred during the second cycle to 3.0% drift. Unlike for Wall C10, lateral-load failure for Wall A10 was from out-of-plane instability of the wall boundary element (i.e., buckling of the gross section) as shown in

Table 6. Damage progression summary for all test walls

| Drift[a]	C10	A10	A14	A20
0.125% (~0.3%)	Horizontal cracking initiated	Horizontal cracking initiated	Sparse and short horizontal cracks appeared	Very sparse and short horizontal cracks
0.25% (0.5–0.6%)	—	—	Cracking higher up the wall height	—
0.5% (0.90–1.0%)	Cracking spans entire wall height	Cracking spans entire wall height	Cracking spans entire wall height	Cracking spans entire wall height and tensile splitting up to 400 mm height
0.75% (1.2–1.35%)	Tensile splitting in lower 300 mm of end region; 0.2 mm MRC[b]	Tensile splitting at end region up to 600 mm height; Hairline MRC	Tensile splitting cracks up to 400 mm height; 0.3 mm MRC	Spalling up to 800 mm height; Hairline MRC
1.0% (1.6–1.7%)	Tensile splitting to 700 mm height [Fig. 6(a)]; Spalling initiated in lower 100 mm; 1.2 mm MRC	Spalling initiated in lower 200 mm [Fig. 6(b)]; —; 0.5 mm MRC	Existing cracks grow but no new cracks observed; Spalling to 800 mm height [Fig. 6(c)]; 0.5 mm MRC	Splitting cracks up to 1,100 mm height [Fig. 6(d)]; Spalling to 300 mm along the length; 0.3 mm MRC
1.5% (2.1–2.2%)	Spalling up to 1,000 mm [Fig. 7(a)]; No confined core damage and no new cracks observed; 2.0 mm MRC	Spalling up to 800 mm [Fig. 7(b)]; No confined core damage and no new cracks observed; 0.6 mm MRC	Spalling up to 1,200 mm height and 400 mm along the length of wall [Fig. 7(c)]; No confined core damage; 1.2 mm MRC	Spalling to 1,300 mm height [Fig. 7(d)]; No confined core damage and no new cracks observed; 0.6 mm MRC
2.0% (2.7–2.8%)	Spalling spreads into confined core and extends 400 mm along the length of the wall; Slight bulging of longitudinal reinforcement. Cracks no longer growing in length; 2.5 mm MRC	Spalling spreads into confined core and extends 400 mm along the length of the wall; Tensile splitting to 1,200 mm. No reinforcement damage; 2.5 mm MRC	Spalling up to 1,300 mm height and 500 mm along the wall length; Bulging of longitudinal reinforcement; 2.5 mm MRC; N/A	First cycle: Spalling extends to 700 mm along wall length; No reinforcement damage. Crushing extends into confined core; 1.4 mm MRC; N/A
3.0% (3.7–3.8%)	Longitudinal reinforcement bulged further but no loss of strength	Longitudinal reinforcement buckled on first cycle to −3.0% drift leading to slight reduction in lateral strength		
Lateral-load failure	Simultaneous confined core crushing and reinforcement buckling on negative cycle at −3.1% drift [Fig. 8(a)]	Global buckling of end region on second cycle to 3.1% [Fig. 8(b)]; Gradual lateral strength loss to zero but full axial load maintained	Simultaneous confined core crushing and highly localized reinforcement buckling on at 2.5% [Fig. 8(c)]; Crushing zone between 300 mm and 700 mm above the foundation. Axial load maintained.	Second cycle: Simultaneous core crushing and reinforcement buckling at 2.0% resulting in 34% strength loss [Fig. 8(d)]; Out-of-plane displacement of 25 mm
Monotonic/Axial failure	Reduction in lateral strength due to reinforcement buckling; Multiple fractures of longitudinal reinforcement; Axial compression failure at 2.4%	Two fractures of longitudinal reinforcement; —; Axial compression failure at −3.0%	Multiple fractures of longitudinal reinforcement; Significant reduction in lateral strength. Axial compression failure at −3.4%; Out-of-plane movement of approximately 10 mm	Simultaneous confined core crushing and reinforcement buckling followed by axial compression failure at 0.85% drift in the positive direction and 0.6% drift in the negative direction

[a]Values in parentheses indicate the calculated drift at the effective height.
[b]MRC = maximum residual crack–crack width after unloading to zero force at this drift level.
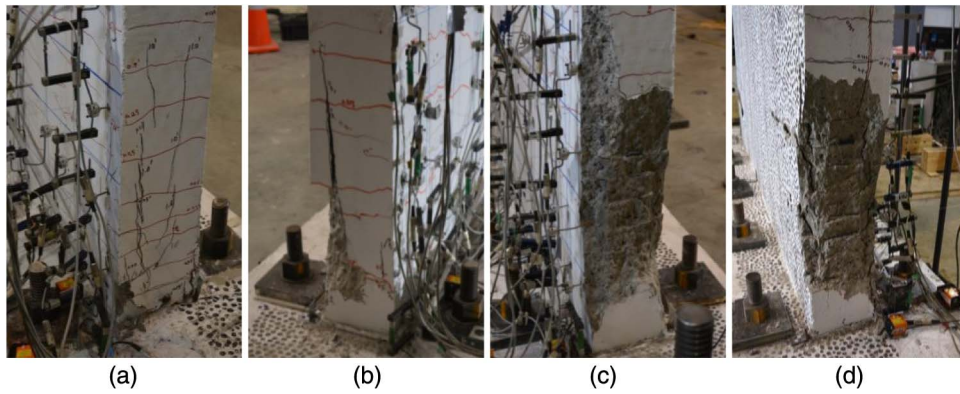
Fig. 6. Damage at boundary element after completion of all cycles at 1.0% drift: (a) C10; (b) A10; (c) A14; and (d) A20.
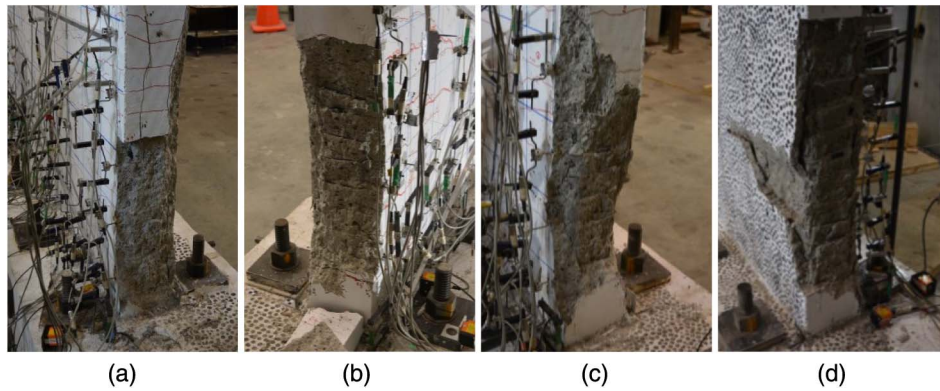
Fig. 7. Damage at boundary element after completion of all cycles at 1.5% drift: (a) C10; (b) A10; (c) A14; and (d) A20.
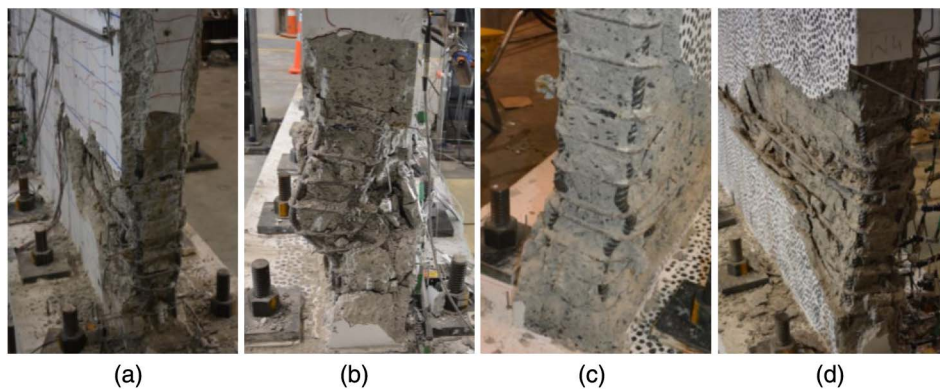
Fig. 8. Damage at boundary element after lateral-load failure (3.1, 3.1, 2.5, and 2.0% drift, respectively): (a) C10; (b) A10; (c) A14; and (d) A20.

Fig. 8(b). Paulay and Priestley (1993) concluded that out-of-plane failure occurs because of excessive tensile strain in reinforcement that inhibits symmetric crack closure, leading to uneven stress distribution through the thickness of the wall. As evident in Fig. 9(b), lateral strength loss from out-of-plane instability in Wall A10 occurred more gradually with increasing drift demand than did lateral-strength loss from compression failure as in Walls C10, A14, and A20. Similar to Wall C10, Walls A14 and A20 experienced lateral-load failures because of simultaneous crushing of the confined concrete and buckling of longitudinal reinforcement in the wall boundary element, at drifts of 2.5 and 2.0%, respectively.

Axial Failure

After initial lateral-load failure, the loading direction was reversed, regardless of whether the desired drift was attained or not. Axial failure was characterized by sudden and unrecoverable loss of both lateral- and axial-load-carrying capacity through simultaneous crushing and reinforcement buckling in the wall boundary element and web. With the exception of Wall C10, which was returned to 0% drift before full axial load was reapplied [dashed line in Fig. 9(a)], all walls maintained full axial load on the reverse cycle from the point of lateral-load failure, indicating that axial load was redistributed from the damaged boundary element to the
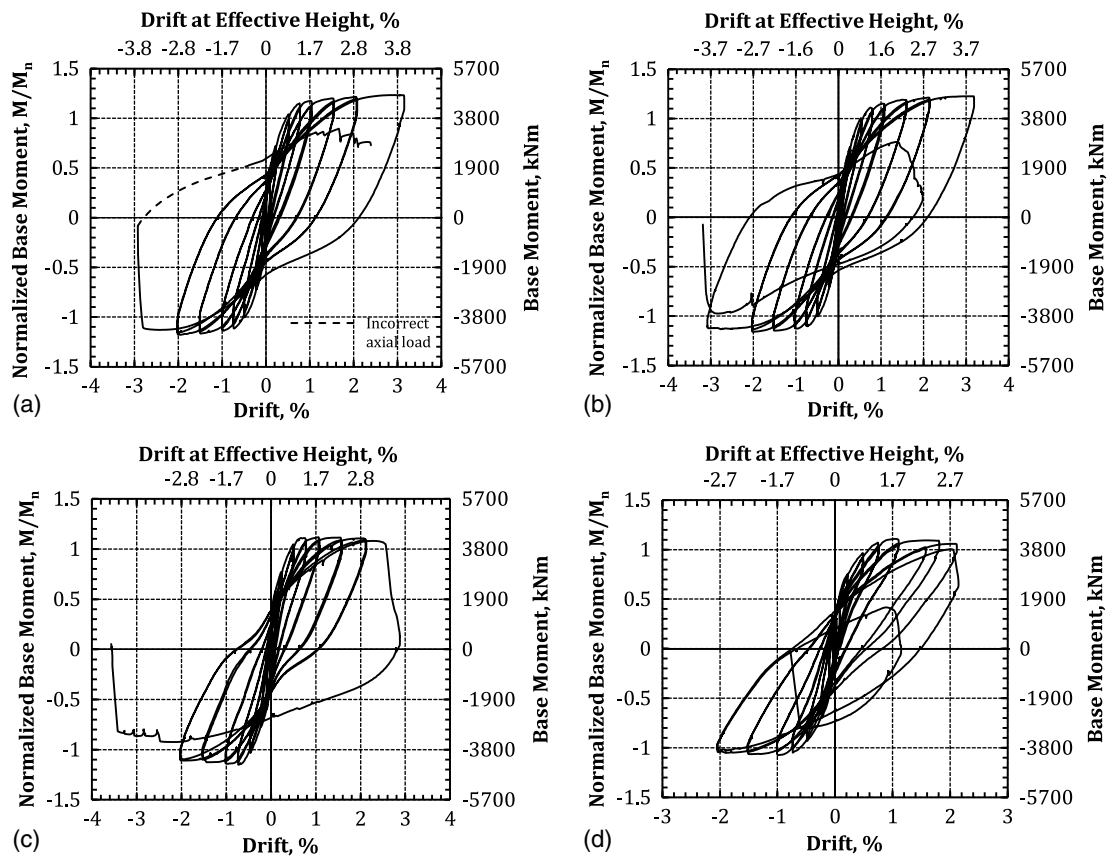
Fig. 9. Base moment versus drift for all test walls: (a) C10; (b) A10; (c) A14; and (d) A20.

less-damaged central portion of the wall. On load reversal, following lateral-load failure, Wall C10 exhibited axial failure at a drift of 2.4% following sequential fracture of five longitudinal reinforcement bars in the tensile boundary element.

Following lateral-load failure for Walls A10 and A14, axial load was maintained for the duration of the monotonic push in the reverse direction until axial failure at −3.0% [Fig. 9(b)] and −3.4% [Fig. 9(c)] drift, respectively. For Wall A20, the target drift of −2.0% was reached following lateral-load failure at 2.0% drift and the loading was reversed twice more resulting in further damage at 1.0% drift and an axial failure at −0.6% drift [as shown in Fig. 9(d)]. Therefore, with the exception of Wall A20, all walls experienced axial failure in the reverse loading direction during the loading excursion immediately following lateral-load failure. Axial failure, therefore, is classified as a secondary failure mode in these walls, occurring soon after initial failure due to loss of lateral-load-carrying capacity.
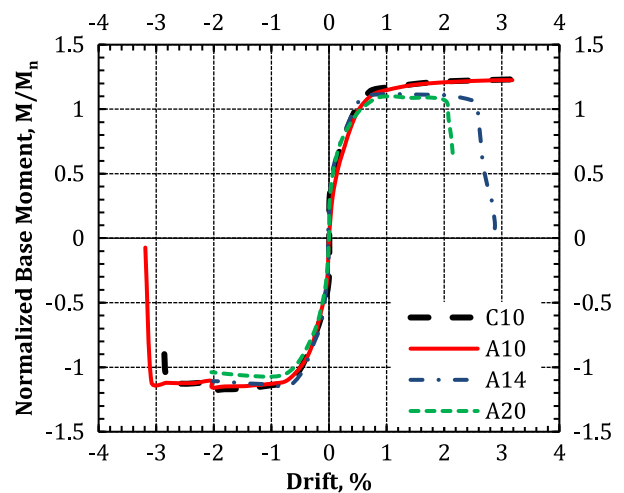
Impact of Study Parameters on Deformation Capacity

Length of Confined Region and Restraint of Web Reinforcement

Backbones for Walls C10 and A10 are shown in Fig. 10. The boundary element in Wall C10 had a confined length that extended to 70% of the neutral axis depth while the confined length of Wall A10 was 100% of the neutral axis depth. These detailing differences did not affect the ultimate drift capacity, although Wall A10 sustained an additional one-half cycle at 3.0% drift. Severe

Fig. 10. Backbone curves for Walls C10, A10, A14, and A20.

buckling of the corner longitudinal reinforcement occurred in both walls. No significant differences were observed with regard to the extent of concrete core damage or spalling throughout the test.

Since no longitudinal web reinforcement buckled prior to wall lateral-load failure, the effectiveness of the crossties on the web longitudinal reinforcement in Walls A10, A14, and A20 is not clear from the results of this study. Strain data from instrumented web crossties indicated low strain demands, typically below 10%

Table 7. Summary of peak test values

Wall	$\dfrac{P}{A_g f'_{c,test}}$	Δ_{cr} (%)	$M_{base,avg}$ (kNm)[a]	$\dfrac{M_{base,avg}}{M_n}$	$\dfrac{M_{top}[b]}{M_y}$	$\dfrac{V_u}{V_n}$	Δ_y (%)[c]	Δ_u (%)[d]	Δ_{u_eff} (%)[e]	θ_p (%)
C10	0.09	0.125	4,622	1.2	0.80	0.35	No data	3.1	3.8	3.4
A10	0.09	0.125	4,580	1.2	0.80	0.35	0.35	3.1	3.7	3.2
A14	0.14	0.25	5,420	1.1	0.71	0.40	0.46	2.5	3.1	2.7
A20	0.20	0.25	6,154	1.1	0.67	0.42	0.31	2.0	2.7	2.1

[a]$M_{base,avg}$ is the average of the peak positive and negative base moments.
[b]Maximum applied moment at the top of the wall, normalized by the calculated yield moment.
[c]Drift at which the outermost longitudinal reinforcement first yielded.
[d]Drift at which the base moment drops below 80% of the peak base moment.
[e]Calculated drift capacity at the effective height.

of the yield strain, prior to lateral-load failure. The shear stress demands in the walls tested as part of this program were low ($<0.21\sqrt{f'_c}$ MPa), and this might have contributed to the low demands on the web crossties. Previous experimental testing (Hube et al. 2014; Kuang and Ho 2008) of walls with higher shear stress demands have shown web crossties to increase wall deformation capacity. Additionally, analytical models by Whitman (2015) have shown that high compression stresses in the web of walls can manifest as a result of the formation of diagonal compression struts [particularly in walls with a small height-to-length (aspect) ratio and a high shear demand]; for these cases, web crossties and a deeper confined region provide confinement that could potentially prevent or delay the onset of diagonal compression failure.

Axial Load Ratio

The ultimate moment to nominal moment ratio was similar for all four walls, ranging from 1.1 to 1.2, as shown in Table 7. The reduction in ultimate drift capacity from Wall A10 to Wall A14 and Wall A14 to Wall A20 was proportional to the increase in axial load. Specifically, an increase in axial load of 43–50% between the test walls corresponded to an ultimate drift capacity reduction of 20% in both pairs. The increase in axial load also increased strength, with the increase in shear stress demand shown in Table 3. Despite this increase, the shear demand-to-nominal capacity ratios in Table 7, V_u/V_n, were all under 0.5 (shear stress $<0.21\sqrt{f'_c}$ MPa), such that any change in wall performance from shear-flexure interaction is considered negligible.

The normalized backbones in Fig. 10 matched closely leading up to section yielding, indicating that the drift at which the section yields is independent of the section strength (and axial load by association) as previous studies have suggested (Priestley 2000; Priestley and Kowalsky 1998). The normalized plots in Fig. 10 also demonstrate that effective section stiffness is influenced by the magnitude of the applied axial load. Unlike NZS 3101:2006-A3, this dependence is not reflected in effective stiffness expressions in ACI-318-14 or ASCE 41-13.

From Figs. 6–8 and descriptions in Table 6, it is clear that axial load influenced the extent of concrete damage up the height and along the length of the walls throughout the test. However, axial load did not appear to have influenced the location of the concentrated concrete crushing that lead to lateral-load failure. Observations, as well as average strain measurements, indicate that concentrated crushing damage consistently occurred between 300 and 700 mm above the base of the wall. Considerably less boundary element damage was observed below 300 mm, possibly from the strength enhancement provided by the confining effect of the foundation.

Fig. 11. Damage to hoop and crosstie confinement in the localized failure regions of A10.

Table 8. Number of fractures in each end of the wall after failure

Wall	C10	A10	A14	A20
Hoop fractures	8	10	14	5
Crosstie fractures	5	0	13	3
Confinement in boundary element of initial crushing	Hoops	Crossties	Crossties	Crossties

Confinement Type (Crossties versus Hoops)

Each wall was detailed with hoops at one end and a combination of hoops and crossties at the other end (Fig. 4). Transverse reinforcement was extracted from the walls after testing; a typical set of samples is shown in Fig. 11. A larger number of hoop fractures, compared to crosstie fractures, were observed in all walls, as summarized in Table 8. The crossties were prone to unbending of the 180° hooks during buckling of the longitudinal reinforcement as the boundary element crushed. Fracture might suggest that the hoops were utilized to their maximum potential, whereas some of the crossties were limited by opening of the 180° bends. Despite this observation, initial crushing did not consistently occur in the same loading direction for each wall, as noted in Table 8. Similarly, results from compression tests on concrete prisms conducted by Mander et al. (1988) show a similar performance between prisms confined by 180–180° crossties and prisms confined solely by hoops. Results from the four walls tested in this study support the findings of Mander et al. (1988) in that the strength of the boundary element or the wall drift capacity was not altered by the configuration of the transverse reinforcement.

Discussion of Measured Response

Instrumentation was used to monitor local and global deformations. The layout enabled measurement of flexural deformation and shear deformation up the height of the wall, in addition to strain penetration into the foundation. The following sections compare the measured responses for the four walls in the test series.
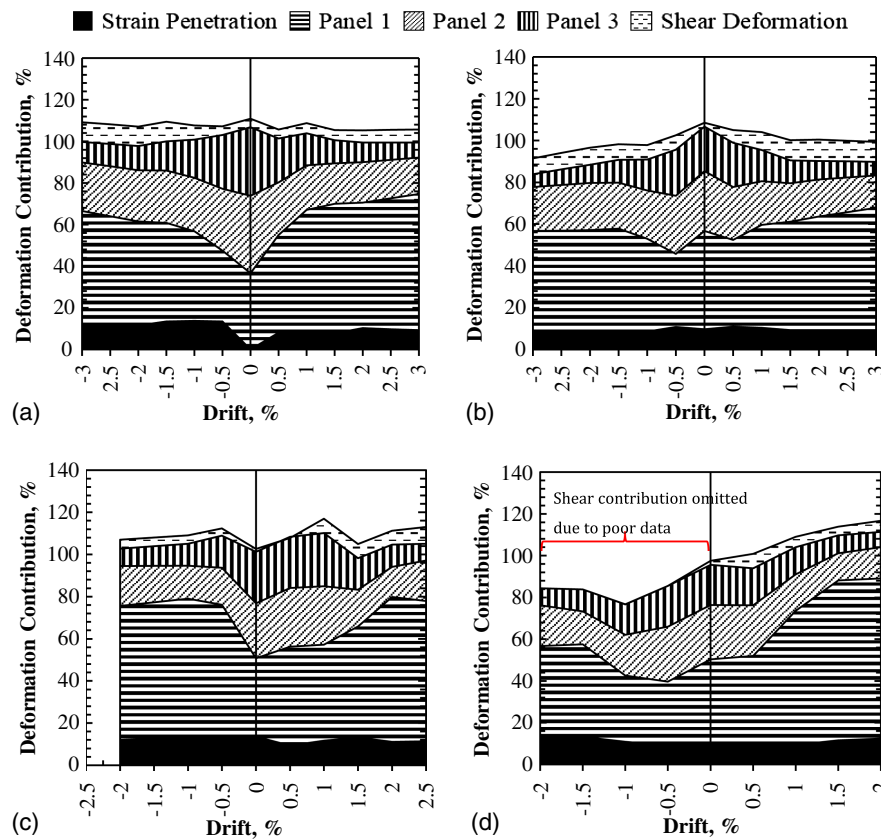
Fig. 12. Components of deformation for all test walls: (a) C10; (b) A10; (c) A14; and (d) A20.

Components of Deformation

Fig. 12 shows the contributions of each component of deformation to the total displacement of the wall. Deformation due to shear sliding along the wall-foundation interface was negligible (<0.5%) and, therefore, is not included in the plots. For all walls, flexural deformation represented 80–90% of the total wall deformation regardless of the axial load ratio. In Fig. 12, flexural bending deformations are further separated into the three panel regions of the wall shown in Fig. 5. From this breakdown it can be seen that 35–50% of the flexural deformation occurred in the lower 1,000 mm (Panel 1) of the walls prior to the approximate yield drift of the section (≤0.5% drift) and increased to 55–70% after yield. Flexural deformation in the upper 2,500 mm of the wall (Panel 2 and 3) ranged between 40 and 50% in the cycles prior to the approximate yield drift and decreased to 22–30% following wall yielding.

Strain penetration of the longitudinal reinforcement at the wall to foundation interface is important to consider in design because it induces higher rotation demands at the base of the wall leading to larger lateral building displacements. Wall rotation from strain penetration occurs at the foundation interface. In the wall tests, the measured wall rotation caused by strain penetration was determined by dividing the difference in displacement measured by sensors PGE and PGW by the distance between these sensors. There is error in this determination of measured rotation at the interface because of the wall curvature over the gauge length of these instruments. Neglecting this error, rigid body rotation from strain penetration contributed 10–15% to the total deformation in all walls and remained relatively constant with increasing drift. The contribution of strain penetration was not influenced by increasing the

axial load ratio. Existing bar slip models (Eligehausen et al. 1983) suggest that strain penetration is dependent on wall length, wall height, longitudinal bar diameter, and material properties. Variation in reported strain penetration contribution among wall testing programs is from the differences in these parameters as well as the aforementioned errors in measurements of rotation at the interface.

Because the shear stress demand was low for the walls, the contribution of shear deformations to total deformation could be expected to be small. The shear deformation represented at most 10% of the total wall deformation. For all walls, the shear contribution increased throughout the test, likely caused by increasing shear force and, in the post-yield range, wider opening of diagonal cracks. For Walls C10 and A10, shear deformation increased from 5% of the total deformation in the initial cycles to a maximum value of 10% at 3.0% drift. For Walls C10 and A10, shear deformation contribution increased from 1–2% in the early cycles to 7–8% at cycles near lateral-load failure. These results suggest that the change in the contribution of shear deformation to the total deformation is negligible between axial load ratios of 0.1 and 0.2. The contribution of shear deformation to total deformation for the walls tested in this study was low in comparison to other wall tests with heavily reinforced boundary elements, including Tran and Wallace (2015) (shear contribution of up to 50%) and Lowes et al. (2012) (shear contribution of up to 30%). The small shear deformations observed in this study were likely due to low shear stress demands and were consistent with data for the lightly reinforced walls tested by Lu et al. (2017), which had similarly low shear stress demands ($<0.21\sqrt{f_c'}$ MPa) and a corresponding shear deformation contribution of under 5%.
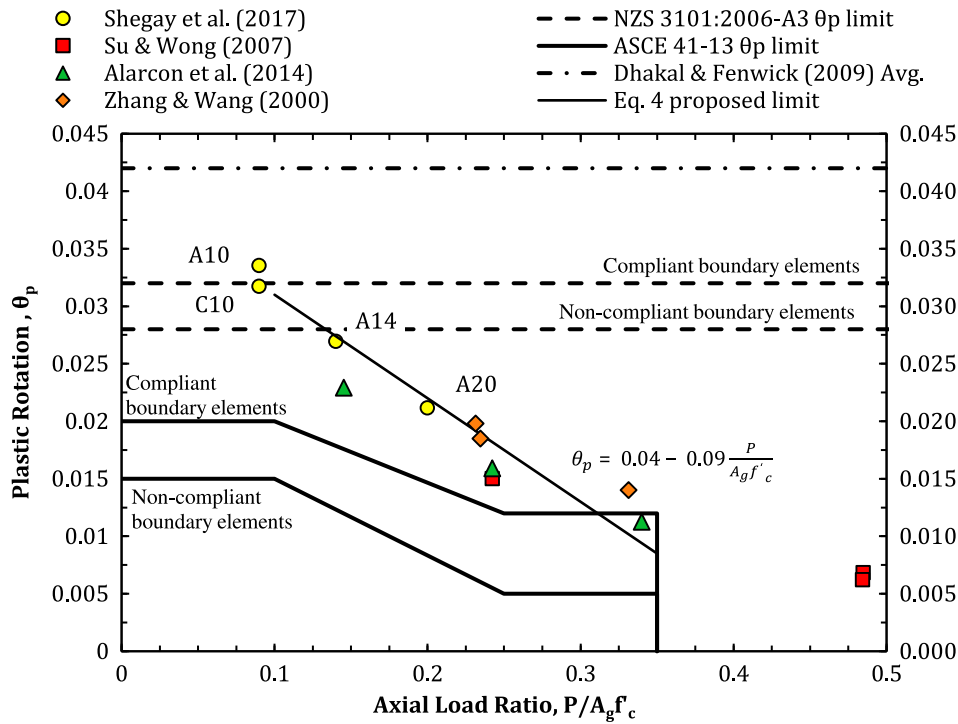
Fig. 13. Measured plastic rotation in test walls compared to limits in NZS 3101:2006-A3 and ASCE 41-13.

Comparison of Plastic Hinge Rotation Capacity to Codified Deformation Limits

Deformation limits in ASCE 41-13 (ASCE 2014) and NZS 3101:2006-A3 (NZS 2017) are expressed in terms of plastic hinge rotation and curvature, respectively. These parameters are related in Eq. (1) by idealizing the rotation to occur at a single point located $L_p/2$ above the point of maximum moment, where L_p is the plastic hinge length, assumed to be $0.5L_w$:

$$\phi_u = \frac{\theta_p}{L_p} + \phi_y \quad \text{where } \theta_p = \frac{\delta_u - \delta_y}{H_{\text{eff}} - L_p/2} \qquad (1)$$

where δ_u and δ_y = ultimate and yield displacements at the effective height (H_{eff}), respectively; ϕ_y = yield curvature; and ϕ_u = ultimate curvature. Since only the lower two stories of the wall were tested in this study, the ultimate displacement at the effective height was estimated using an effective stiffness of $0.35EI_g$. Yield displacement was calculated by double integrating the estimate for yield curvature, given in Eq. (2), over the effective height of the wall

$$\phi_y = \frac{2f_y}{E_s L_w} \qquad (2)$$

where E_s = Young's modulus of the longitudinal reinforcement; and f_y is taken as the measured yield stress of the reinforcement from tensile tests (not exceeding 425 MPa) (Priestley and Kowalsky 1998). The resulting plastic rotations for each wall are summarized in Table 7.

In the United States, ASCE 41-13 (ASCE 2014) contains limits on plastic rotation capacity (referred to as parameter b) to be used as acceptance criteria when analyzing wall segments. The limits are plotted against the axial load ratio in Fig. 13 for shear stress demands less than $0.33\sqrt{f'_c}$ MPa. In comparison, NZS 3101:2006-A3 specifies the deformation limit as a maximum

curvature ductility limit, $K_d = \phi_u/\phi_y$, which depends on the classification of the plastic hinge region (nominally ductile, limited ductile, or ductile) and the presence of boundary elements but does not take into account the influence of loading or the degree of detailing. The New Zealand code limits were derived based on a lower-bound of the average curvatures attained from seven ductile wall tests conducted in New Zealand (Dhakal and Fenwick 2008). In this paper, the average and the adopted (i.e., lower bound) curvature limits were translated to plastic rotation by substituting Eq. (2) into Eq. (1), assuming $L_p = 0.5L_w$, and rearranging to produce:

$$\theta_p = (K_d - 1)\frac{f_y}{E_s} \qquad (3)$$

Fig. 13 compares the average value as derived by Dhakal and Fenwick (2008), the NZS 3101:2006-A3 limits, and the ASCE 41-13 limits for walls with low shear stress demands ($\leq 0.33\sqrt{f'_c}$ MPa). From this figure, it is evident that NZS 3101:2006-A3 permits ductile walls to develop significantly larger plastic rotations than ASCE 41-13, particularly at high axial loads.

The derived plastic rotation values from the tests in this study and previous tests reported in Table 1 (spanning a total wall length range of 400–2,250 mm) are also plotted in Fig. 13. All of the data points fall below the average plastic rotation limits reported by Dhakal and Fenwick (2008). Maximum plastic rotations for Walls C10 and A10 prior to failure are 20% below this average and are roughly equal to the NZS 3101:2006-A3 limit. These rotations are 60% larger than the upper deformation limits specified in ASCE 41-13. The plastic rotations for A14 and A20 are 16 and 33% below the NZS 3101:2006-A3 limit, respectively. A linear trendline for plastic rotation capacity is fit through the data points in Fig. 13 below a practical upper bound axial load ratio of 0.5, resulting in the following expression for plastic hinge capacity in terms of axial load ratio:

$$\theta_p = 0.04 - 0.09\left(\frac{P}{A_g f'_{c,test}}\right) \qquad (4)$$

assuming a plastic hinge length of $0.5L_w$ and a yield curvature determined using Eq. (2). The rotation limit in Eq. (4) can also be approximately expressed as a limit on curvature ductility as follows:

$$K_d = \phi_u/\phi_y = 20 - 45\left(\frac{P}{A_g f'_{c,test}}\right) \qquad (5)$$

Using this trend, a plastic rotation capacity of 1.3% is estimated at an axial load ratio limit of 0.3, the limit in NZS 3101:2006-A3. This extrapolated value of 1.3% is approximately 60% lower than the plastic rotation limit in NZS 3101:2006-A3 and approximately equal to the limit in ASCE 41-13 for walls with confined boundary elements. From Fig. 13 it is evident that current plastic rotation limits in NZS 3101:2006-A3 are unconservative for rectangular walls with axial load ratios in excess of 10%, with the lack of conservatism increasing as axial load ratio increases. From these results it is apparent that constant curvature/rotation limits, as used in NZS 3101:2006-A3, are not appropriate, and such limits should depend on other variables including the applied axial load ratio. The wall tests in Fig. 13 satisfy slenderness provisions of NZS 3101:2006-A3 and have thickness values that were 80–100% of that required by ACI 318-14, which are intended to prevent failure from lateral instability of the section. The performance of thinner walls (such as ordinary walls or those designed to nominal ductility) may not be captured accurately by Eq. (4). As with all empirical models, caution should be used in applying this model to walls with design parameters beyond the range of parameters represented in the database.

Although the ASCE 41-13 limits are generally more conservative than the NZS 3101:2006-A3 limits when compared to the test data in Fig. 13, a detailed study on a database of wall tests by Birely et al. (2014) demonstrated that the plastic hinge rotation capacity is sensitive to changes in axial load ratio between 0.02 and 0.1 and that the ASCE 41-13 limits can be unconservative for walls with axial load ratios above 0.1. It was also shown in this study that while shear stress demand and the level of confinement are currently accounted for in the ASCE 41-13 plastic rotation limits, the true influence of these parameters on the plastic hinge rotation capacity is poorly captured.

Summary and Conclusions

Four one-half-scale RC walls were tested under constant axial load and cyclic lateral loading to evaluate the effects of (i) detailing of boundary element and web transverse reinforcement and (ii) low to moderate axial load on wall performance. Wall C10 was designed with conventional detailing according to NZS 3101:2006-A2, while Wall A10 was detailed to the augmented provisions in NZS 3101:2006-A3 and included an extended boundary element length (extending the full length of the neutral axis depth) and crossties in the web. Walls C10 and A10 were tested at an axial load ratio of 0.10 and Walls A14 and A20 were tested at higher axial load ratios of 0.14 and 0.2, respectively. Deformation capacity was compared among the walls and to existing limits in ASCE 41-13 and NZS 3101:2006-A3. The following key observations were made:

1. Walls C10 (confinement extending to 70% of the neutral axis depth) and A10 (confinement extending to 100% of the neutral axis depth) attained plastic hinge rotation capacities of 3.4 and

3.2%, respectively. Test walls subjected to higher axial load ratios of 14% (A14) and 20% (A20) attained plastic hinge rotation capacities of 2.7 and 2.1%, respectively, and lost lateral-load-carrying capacity through simultaneous crushing of the boundary element and buckling of longitudinal reinforcement. Increasing axial load corresponded to increased concrete damage up the height and along the length of the walls throughout the tests. The reported plastic hinge rotation capacity of each wall was in excess of the measured drift for that wall because the center of plastic rotation was located above the base of the wall.

2. In all walls, the full axial load was sustained following lateral-load failure. However, the residual deformation capacity between lateral-load failure and axial failure was limited to a single additional drift cycle at most. For Walls C10 and A10, axial failure occurred at measured drifts of 2.4 and 3.0%, respectively, which was no more than a one-half cycle beyond lateral-load failure (which occurred at measured drifts of 3.1% for both walls). Wall A14 experienced axial failure at a measured drift of 3.4% after lateral-load failure at a measured drift of 2.5% in the previous cycle. Wall A20 could not sustain larger drift demands beyond lateral-load failure (at 2.0% measured drift) before experiencing axial failure.

3. The breakdown of deformation components indicate that the behavior of all four walls was dominated by flexure. Shear deformations contributed 3–10% of the total deformation throughout the tests, and were not significantly affected by different axial load ratios. The shear contributions were small compared to similar tests in the literature, and this was attributed to low shear stress demand resulting from capacity design requirements in NZS 3101:2006-A3.

4. At the conclusion of the tests, it was observed that more hoop legs of transverse reinforcement had fractured than did crossties, which were more prone to unbending of the 180–180° hooks; however, these differing failure modes did not affect the strength of the boundary elements.

5. The deformation capacity of the plastic hinge in Walls C10 and A10 just satisfied the current NZS 3101:2006-A3 deformation limits, while the ASCE 41-13 limit was much smaller than the measured values. At the higher axial load ratios in A14 and A20, the deformation capacity of the plastic hinge reduced considerably to approximately 16 and 33% below the deformation limits in NZS 3101:2006-A3, respectively. Extrapolation of the test results suggests that the deformation capacity of the plastic hinge at the newly adopted axial load ratio limit of 0.3 is approximately 60% below the allowable limits in NZS 3101:2006-A3 and approximately equal to the limits in ASCE 41-13.

Based on the last observation, it was concluded that the plastic rotation capacity of rectangular walls designed at or near an axial load ratio of 0.3, the new limit in NZS 3101:2006-A3, is far below the permitted rotational limits in NZS 3101:2006-A3, even when designed using detailing provisions for ductile-class walls. This may lead to nonductile failure of the wall at significantly lower than expected drifts. A recommended alternative is to redefine the plastic rotation limits to be conditional on the axial load (among other parameters), as is done in ASCE 41-13. Based on this study, it is recommended that plastic rotation capacity of rectangular walls with low shear stress demands be estimated using Eq. (4).

Acknowledgments

Innovation and Employment. The authors would also like to acknowledge the assistance provided by Craig Stevenson, Des Bull, Rick van Ballegooy, Ashley Smith, and Weng Yuen Kam in wall design and Ross Reichardt, Mark Byrami, Mark Twiname, Andrew Virtue, Jay Naidoo, Shane Smith, Lucas Hogan, Vadim Shegay, Sean Lawrence, Enoch Korapatti, and Margaux Delair during wall construction and testing.

References

ACI (American Concrete Institute). 2014. *Building code requirements for structural concrete and commentary*. ACI 318-14. Famington Hills, MI: ACI.

ACI Innovation Task Group 5. 2007. *Acceptance criteria for special unbonded post-tensioned precast structural walls based on validation testing and commentary*. Famington Hills, MI: ACI.

Alarcon, C., M. A. Hube, and J. C. de la Llera. 2014. "Effect of axial loads in the seismic behavior of reinforced concrete walls with unconfined wall boundaries." *Eng. Struct.* 73: 13–23. https://doi.org/10.1016/j.engstruct.2014.04.047.

Arteta, A. C. 2015. "Seismic response assessment of thin boundary elements of special concrete shear walls." Ph.D. dissertation, Univ. of California.

ASCE. 2014. *Seismic evaluation and retrofit of existing buildings (ASCE/SEI standard 41-13)*. ASCE 41. Reston, VA: ASCE.

Birely, A. C., D. E. Lehman, and L. N. Lowes. 2014. "Evaluation of ASCE 41 modeling parameters for slender reinforced concrete structural walls." *ACI Spec. Publ.* 297 (4): 1–18.

CERC (Canterbury Earthquakes Royal Commission). 2012. Vol. 2 of *The performance of Christchurch CBD buildings*. Christchurch, New Zealand: Canterbury Earthquakes Royal Commission.

Chilean Structural Standard. 2010. "Reinforced concrete design code, replacing D.S N 118." DS 60 MINVU. [In Spanish.] Santiago, Chile: Chilean Ministry of Housing and Urbanism, Diario Official.

CSA (Canadian Standards Association). 2004. "Design of concrete structures." CSA A23.3-04. Mississauga, ON, Canada: CSA.

Deng, M., X. Liang, and K. Yang. 2008 "Experimental study on seismic behavior of high performance concrete shear wall with new strategy of transverse confining stirrups." In *Proc., 14th World Conf. on Earthquake Engineering*, 1–8. Tokyo: International Association for Earthquake Engineering.

Dhakal, R. P., and R. C. Fenwick. 2008. "Detailing of plastic hinges in seismic design of concrete structures." *ACI Struct. J.* 105 (6): 742–745.

Dunning Thornton Consultants Ltd. 2011. *Report on the structural performance of the Hotel Grand Chancellor in the earthquake on 22 February 2011*. Wellington, New Zealand: Dept. of Building and Housing.

Eligehausen, R., E. P. Popov, and V. V. Bertero. 1983. *Local bond stress-slip relationships of deformed bars under generalized excitations*. Rep. No. UCB/EERC-83/23. Berkeley, CA: Univ. of California.

Hilson, C. W. 2014. "Analytical and experimental studies of the seismic performance of reinforced concrete structural wall boundary elements." Ph.D. dissertation, Univ. of California.

Hube, M. A., A. Marihuén, J. C. la Llera, and B. Stojadinovic. 2014. "Seismic behavior of slender reinforced concrete walls." *Eng. Struct.* 80: 377–388. https://doi.org/10.1016/j.engstruct.2014.09.014.

Huq, M. S., A. Lepage, R. D. Lequesne, and S. Ameen. 2017. "Influence of mechanical properties of high-strength steel on deformation capacity of reinforced concrete walls." In *Proc., 16th World Conf. on Earthquake Engineering*, 1–8. Tokyo: International Association for Earthquake Engineering.

Kuang, J. S., and Y. B. Ho. 2008. "Seismic behavior and ductility of squat reinforced concrete shear walls with nonseismic detailing." *ACI Struct. J.* 105 (2): 225–232.

Lowes, L. N., D. E. Lehman, A. C. Birely, D. A. Kuchma, K. P. Marley, and C. R. Hart. 2012. "Earthquake response of slender planar concrete walls with modern detailing." *Eng. Struct.* 43: 31–47. https://doi.org/10.1016/j.engstruct.2012.04.040.

Lu, Y., R. S. Henry, R. Gultom, and Q. T. Ma. 2017. "Cyclic testing of reinforced concrete walls with distributed minimum vertical reinforcement." *J. Struct. Eng.* 143 (5): 1–17. https://doi.org/10.1061/(ASCE)ST.1943-541X.0001723.

Mander, J. B., M. J. N. Priestley, and R. Park. 1988. "Observed stress-strain behavior of confined concrete." *J. Struct. Eng.* 114 (8): 1827–1849. https://doi.org/10.1061/(ASCE)0733-9445(1988)114:8(1827).

New Zealand Concrete Society. 1998. *Red Book: Section B3 structural walls*. Wellington, New Zealand: New Zealand Concrete Society.

NIST (National Institute of Standards and Technology). 2014. *Recommendations for seismic design of reinforced concrete wall buildings based on studies of the 2010 Maule, Chile earthquake*. NIST GCR 14-917-25. Gaithersburg, MD: NIST.

NZS (Standards New Zealand). 2004. *Structural design actions part 5: Earthquake actions: New Zealand*. NZS 1170.5:2004. Wellington, New Zealand: Standards New Zealand.

NZS (Standards New Zealand). 2012. *Concrete structures standard. Part 1: The design of concrete structures (Amendment No. 2)*. NZS 3101:2006. Wellington, New Zealand: Standards New Zealand.

NZS (Standards New Zealand). 2017. *Concrete structures standard. Part 1: The design of concrete structures (Amendment No. 3)*. NZS 3101:2006. Wellington, New Zealand: Standards New Zealand.

Paulay, T., and M. J. N. Priestley. 1993. "Stability of ductile structural walls." *ACI Struct. J.* 90 (4): 385–392.

Priestley, M. J. N. 2000. "Performance based seismic design." *Bull. New Zealand Soc. Earthquake Eng.* 33 (3): 325–346.

Priestley, M. J. N., and J. M. Kowalsky. 1998. "Aspects of drift and ductility capacity of rectangular cantilever structural walls." *Bull. New Zealand Soc. Earthquake Eng.* 31 (2): 73–85.

SESOC (Structural Engineering Society). 2013. *Interim design guidance: Design of conventional structural systems following the canterbury earthquakes*. Wellington, New Zealand: Structural Engineering Society New Zealand, Inc.

Shegay, A. V., C. J. Motter, R. S. Henry, and K. J. Elwood. 2015 "A database for investigating NZS3101 structural wall provisions." In *Proc., 10th Pacific Conf. on Earthquake Engineering*, Melbourne, Australia: Australian Earthquake Engineering Society.

Shegay, A. V., C. J. Motter, R. S. Henry, and K. J. Elwood. 2018. "University of Auckland Ductile Wall Experimental Program." Accessed September 1, 2017. https://doi.org/10.17603/ds22951.

Su, R. K. L., and S. M. Wong. 2007. "Seismic behaviour of slender reinforced concrete shear walls under high axial load ratio." *Eng. Struct.* 29 (8): 1957–1965. https://doi.org/10.1016/j.engstruct.2006.10.020.

Tran, T. A., and J. W. Wallace. 2015. "Cyclic testing of moderate-aspect-ratio reinforced concrete structural walls." *ACI Struct. J.* 112 (6): 653–666.

Welt, T. S., L. M. Massone, J. Lafave, D. E. Lehman, S. L. McCabe, and P. Polanco. 2017. "Confinement behavior of rectangular reinforced concrete prisms simulating wall boundary elements." *J. Struct. Eng.* 143 (4): 1–12. https://doi.org/10.1061/(ASCE)ST.1943-541X.0001682.

Whitman, Z. J. 2015. "Investigation of seismic failure modes in flexural concrete walls using finite element analysis." M.S. thesis, Univ. of Washington.

Zhang, Y., and Z. Wang. 2000. "Seismic behavior of reinforced concrete shear walls subjected to high axial loading." *ACI Struct. J.* 97 (5): 739–750.